Elastic Anisotropic and Thermodynamic Properties of Two BC_7 Phases

Mengjiang Xing*, Binhua Li, Zhengtao Yu and Qi Chen
Faculty of Information Engineering and Automation, Kunming University of Science and Technology, Kunming, 650051, PR China

(Received December 25, 2016; in final form June 21, 2017)

The structural, elastic, anisotropic, and thermodynamic properties of $P3m1$-BC_7 and $Pmm2$-BC_7 have been studied in this paper utilizing first-principles calculations. In comparison with the elastic properties of $Pmm2$-BC_7, $P3m1$-BC_7 exhibits slightly higher values in bulk modulus and B/G, with similar values in shear modulus, the Young modulus, and the Poisson ratio. The calculated Pugh modulus ratio (B/G) and the Poisson ratio demonstrates $P3m1$-BC_7 from brittle to ductile at 93.60 and 93.73 GPa, respectively. Calculations of shear anisotropic factor, universal elastic anisotropy index, shear modulus, the Young modulus, and the Poisson ratio for BC_7 then demonstrate that $Pmm2$-BC_7 exhibits a larger elastic anisotropy than $P3m1$-BC_7. Quasi-harmonic Debye model is finally applied to investigate the Debye temperature, the coefficient of thermal expansion, heat capacity and Grüneisen parameter of $Pmm2$-BC_7 and $P3m1$-BC_7.

DOI: 10.12693/APhysPolA.132.1340

PACS/topics: *ab initio* calculations, elastic properties, anisotropic properties, thermodynamic properties

1. Introduction

Potentials for industrial applications of superhard materials are numerous [1], which leads to an exceptional level of scientific interest. Experimental and theoretical efforts to pursue progressive new superhard materials have motivated studies of boron rich systems [2–10]. Recently, there has been considerable interest on B_xC_y compounds, mainly due to the discovery of its characteristic superconductivity [11, 12]. Extreme Vickers hardness (71 GPa) was claimed in a successfully synthesized diamond-like BC_5 phase [13]. Xu et al. [14] have predicted two novel low-energy structures of BC_7: graphite-like $Amm2$ structure and diamond-like P-$4m2$ structures. Additional findings led to the discovery that diamond-like BC_7 was superconducting with a critical temperature of ≈ 11.4 K and theoretical Vickers hardness was 78.0 GPa, indicating a superhard material. Phase transition pressure from graphite-like to diamond-like was determined to be at 2.2 GPa. Zhang et al. [15] have predicted cubic BC_3 by performing a swarm structure search. Calculated hardness and ideal strength results confirm that cubic diamond-like BC_3 is a superhard material (62 GPa) with deformation modes under tensile and shear strains displaying intriguing bond elongation and sequential bond-breaking processes leading to remarkable extended ductility and elastic response. Utilizing first-principles calculations, Zhao and Wang [16] investigated mechanical properties and electronic structure of the recently synthesized diamond-like BC_5 systematically. Liu et al. [17] discovered a potential superhard material (61.9 GPa) and superconductive materials with superconducting critical temperatures reaching $16.6 \approx 23.4$ K for *Pmma-a* (space group) phase of diamond-like BC_3.

*corresponding author; e-mail: mjxing1686680163.com

Utilizing particle swarm optimization (PSO) methodology for crystal structure prediction, Liu et al. [18] discovered four potential superhard structures of P-$4m2$, $P3m1$, $Pmm2$ and $R3m$, with energetically superior traits to the previously proposed P-$43m$ structure. Previous research has not systematically investigated the new $P3m1$ and $Pmm2$ phase of BC_7, including mechanical, elastic anisotropic and thermodynamic properties, thus detailed first-principles calculations of each for $P3m1$-BC_7 and $Pmm2$-BC_7 based on density functional theory (DFT) under high pressure are studied.

2. Theoretical method

Structural optimization and property predictions of the BC_7 polymorphs were performed in these calculations utilizing DFT [19, 20] with the generalized gradient approximation (GGA) parameterized by Perdew, Burke and Ernzerhof (PBE) [21] and the local density approximation (LDA) [22, 23] as implemented in the Cambridge Serial Total Energy Package (CASTEP) code [24]. Ultrasoft pseudopotential was applied with an energy cutoff of 700, 700, 700, 580, and 620 eV for $P3m1$, $Pmm2$, P-$6m2$, P-$43m$ and P-$4m2$, respectively, and Monkhorst–Pack k-point meshes [25] within 0.025, for the Brillouin zone sampling. Interaction between ions and electrons were described utilizing the Vanderbilt ultrasoft pseudopotentials for B and C with $2s^22p^1$ and $2s^22p^2$ as valence electrons, respectively. Self-consistent onvergence of the total energy is 5×10^{-6} eV/atom, maximum force on the atom is 0.01 eV/Å, maximum ionic displacement is within 5×10^{-4} Å, and the maximum stress is within 0.02 GPa.

3. Results and discussion

3.1. Structural properties

$P3m1$-BC_7 retains a trigonal symmetry related to the $P3m1$ space group, and $Pmm2$-BC_7 retains an orthorhombic symmetry related to the $Pmm2$ space group, respectively. Calculated lattice parameters within GGA

and LDA functionals of $P3m1$-BC_7 and $Pmm2$-BC_7, combined with previous results are displayed in Table I. Calculated lattice parameters for $P3m1$-BC_7 and $Pmm2$-BC_7 are a reasonable comparison [18]. Figure 1 displays the crystal structures of $P3m1$- and $Pmm2$-BC_7. The red and black spheres represent B and C atoms, respectively. Pressure dependence of the equilibrium lattice parameters a/a_0, b/b_0, c/c_0 and V/V_0 (where a_0, b_0, c_0 and V_0 are the equilibrium conventional lattice constants at zero pressure and temperature, respectively) are illustrated in Fig. 2. Compressibility along a-axis for $P3m1$-BC_7 is remarkably easier than along c-axis; however, for $Pmm2$-BC_7, compressibility along b-axis is easier than along a-axis and c-axis. The volume compressions V/V_0 as a function of pressure are also plotted in Fig. 2b for comparison of incompressibility for $P3m1$-BC_7, $Pmm2$-BC_7, c-BN, and diamond under pressure. Incompressibility of $P3m1$-BC_7 and $Pmm2$-BC_7 are demonstrated as slightly less than diamond and slightly larger than c-BN. Table I also presents the calculated equation of state (EOS) for $P3m1$-BC_7 and $Pmm2$-BC_7 under pressures from 0 to 100 GPa. The bulk modulus B and its pressure derivative B_0' are 388.21 (355.82) and 3.70 (4.14) GPa for $P3m1$-BC_7 ($Pmm2$-BC_7) respectively fitted to a third-order Birch–Murnaghan EOS equation [26].

TABLE I

Lattice constants a, b, c [Å], and cell volume per formula unit V_0 [Å^3]. EOS fitted bulk modulus B_0 [GPa] and its derivative B_0' for $P3m1$-BC_7 and $Pmm2$-BC_7 are also shown.

Space group		a	b	c	V	B_0	B_0'
P3m1	GGA[a]	2.5314		8.4996	47.1667	388.21	3.70
	LDA[a]	2.5221		8.3861	46.2001		
	GGA[b]	2.5356		8.5188	47.4305		
Pmm2	GGA[a]	2.5455	5.0925	3.7026	47.9957	355.82	4.14
	LDA[a]	2.5148	5.0301	3.6630	46.3375		
	GGA[b]	2.5132	5.1240	3.6870	47.4798		

[a]This work, [b]Ref [18]

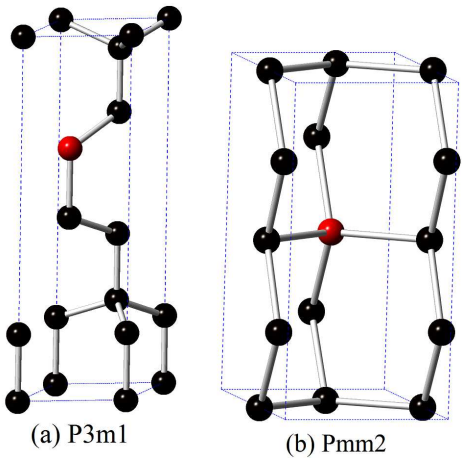

Fig. 1. The crystal structure of $P3m1$-BC_7 (a) and $Pmm2$-BC_7 (b) (black spheres denote carbon atoms, and blue spheres denote boron atoms).

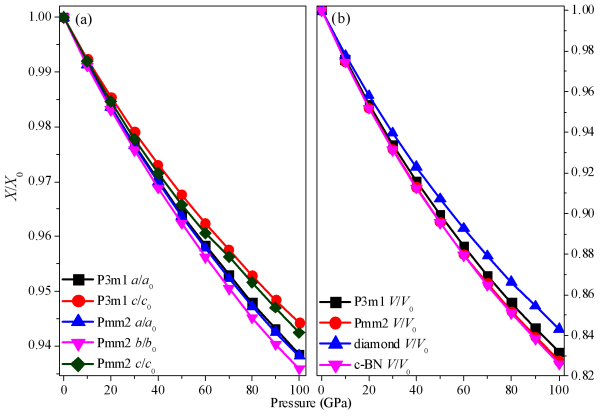

Fig. 2. The lattice constants a/a_0, b/b_0, c/c_0 compression as functions of pressure for $P3m1$-BC_7 and $Pmm2$-BC_7 (a), and primitive cell volume V/V_0 for $P3m1$-BC_7, $Pmm2$-BC_7, c-BN and diamond (b).

3.2. Elastic properties and anisotropy

Elastic properties provide information related to stability and stiffness of materials. Trigonal crystals feature six independent calculated elastic constants (C_{ij}) for $P3m1$-BC_7; however, orthorhombic crystals feature eight independent calculated elastic constants for $P3m1$-BC_7. Calculated results for elastic constants of BC_7 and other structures of BC_7 are presented in Table II with the elastic constants of diamond are also listed for comparison. Elastic modulus of $P3m1$-BC_7, $Pmm2$-BC_7 and diamond were calculated together with previous results for this study as also displayed in Table II. The criteria for mechanical stability of trigonal symmetry group are derived by [27]:

$$C_{ij} > 0,\ i = j = 1 \div 6, \tag{1}$$

$$C_{11} - C_{12} > 0, \tag{2}$$

$$C_{11}C_{33}C_{44} - C_{14}^2C_{33} - C_{13}^2C_{44} > 0, \tag{3}$$

$$C_{11}C_{33} + C_{12}C_{33} - 2C_{13}^2 > 0, \tag{4}$$

$$C_{44}(C_{11} - C_{12}) - 2C_{14}^2 > 0. \tag{5}$$

Criteria for mechanical stability of orthorhombic symmetry group are derived by [28, 29]:

$$C_{ii} > 0, i = 1 \div 6, \tag{6}$$

$$C_{11} + C_{22} + C_{33} + 2(C_{12} + C_{13} + C_{23}) > 0, \tag{7}$$

$$C_{11} + C_{22} - 2C_{12} > 0, \tag{8}$$

$$C_{11} + C_{33} - 2C_{12} > 0, \tag{9}$$

$$C_{22} + C_{33} - 2C_{23} > 0. \tag{10}$$

Elastic constants meet the requirements from Eqs. (1)–(5) and Eqs. (6)–(10), respectively, which indicates that $P3m1$-BC_7 and $Pmm2$-BC_7 are mechanically stable. Phonon spectra are calculated at 0 GPa (Ref. [18]) to ensure stability of $P3m1$-BC_7 and $Pmm2$-BC_7. $P3m1$-BC_7 and $Pmm2$-BC_7 exhibit stability at 0 GPa, as there is no imaginary frequency. The elastic constants and elastic modulus versus pressure for $P3m1$-BC_7 and $Pmm2$-BC_7 are displayed in Fig. 3. Among this bulk modulus, $P3m1$-BC_7 retains

the largest value. The Young modulus E and the Poisson ratio v are expressed as: $E = 9BG/(3B + G)$, $v = (3B-2G)/[2(3B+G)]$. All elastic constants C_{ij} (except for C_{14} and C_{44}) for $P3m1$-BC_7 and elastic modulus increase with different rates under increasing pressure. C_{33} of $P3m1$-BC_7 increases faster than others, and C_{66} exhibits the slowest growth; however, for $Pmm2$-BC_7, all elastic constants C_{ij} and elastic modulus increase under increasing pressure while the difference is C_{11} of $Pmm2$-BC_7 increases faster than others, but C_{66} still exhibits the slowest growth. Observations of Table II reveal that the Young modulus of $P3m1$-BC_7 is smaller than $Pmm2$-BC_7.

TABLE II

Calculated elastic constant C_{ij}, bulk modulus B [GPa], shear modulus G [GPa], the Young modulus E [GPa] and the Poisson ratio v of BC_7 and diamond.

Space group		C_{11}	C_{12}	C_{13}	C_{14}	C_{22}	C_{23}	C_{33}	C_{44}	C_{55}	C_{66}	B	G	E	v
P3m1	GGA[a]	828	239	67	-41	828	67	1101	382	382	295	389	361	827	0.146
	LDA[a]	893	183	53	-52	893	53	1010	293	293	355	378	347	797	0.149
	GGA[b]	830	215	53				1099	377			378	368	834	0.133
Pmm2	GGA[a]	936	10	180		925	152	836	470	460	257	375	383	857	0.119
	LDA[a]	906	-3	162		897	129	803	461	454	258	353	379	937	0.105
	GGA[b]	948		168		975	159	812	493	489	330	377	415	911	0.097
P-43m	GGA[a]	312	419						481			384	52		
P-4m2	GGA[a]	905	88	136				908	424		293	382	382	860	0.125
	GGA[c]	830	166	154				884	500		463				
diamond	GGA[a]	1055	122						566			429	520	1111	0.068
	LDA[a]	1100	138						596			459	545	1171	0.075
	exp.[d]	1076	125						577			422			

[a]This work, [b]Ref [18], [c]Ref [14], [d]Ref [44]

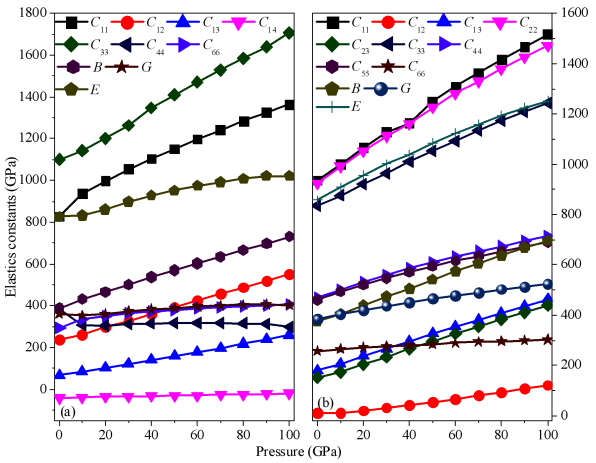

Fig. 3. Elastic constants and elastic modulus of $P3m1$-BC_7 (a) and $Pmm2$-BC_7 (b) as a function of pressure.

The Poisson ratio v of $P3m1$-BC_7 and $Pmm2$-BC_7 are as follows: $v_{P3m1} > v_{Pmm2}$. The Poisson ratio v refers to a ductile compound, usually exhibiting a large v (v>0.26) [30], thus $P3m1$-BC_7 and $Pmm2$-BC_7 are brittle compounds. The B/G is also consistent with v, referring to a ductile compound usually exhibiting a large B/G ratio ($B/G > 1.75$). Thus if $B/G > 1.75$, the material behaves in a ductile manner [31]. Otherwise, the material behaves in a brittle manner. The B/G ratio

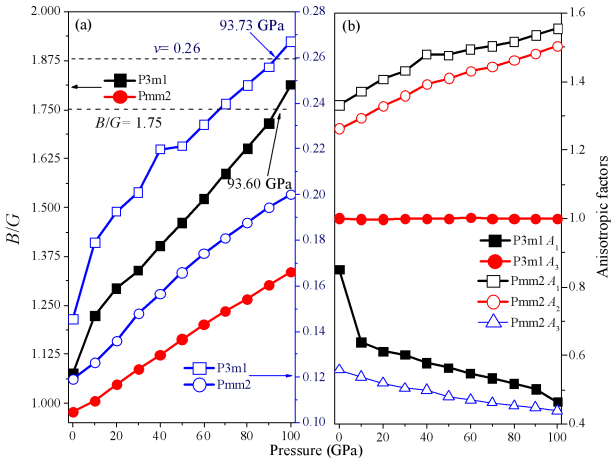

Fig. 4. (a) the Poisson ratio and B/G of $P3m1$-BC_7 and $Pmm2$-BC_7 as a function of pressure, (b) A_1, A_2, A_3 of $P3m1$-BC_7 and $Pmm2$-BC_7 as a function of pressure.

of $P3m1$-BC_7 and $Pmm2$-BC_7 at $P = 0$ GPa are 1.08 and 0.979, respectively, while values of B/G and v for $P3m1$-BC_7 and $Pmm2$-BC_7 are less than 1.75 and 0.26 at 0 GPa, respectively. This indicates a brittle state. The B/G of $P3m1$-BC_7 and $Pmm2$-BC_7 as a function of pressure are presented in Fig. 4a. B/G increases under increasing pressure with $B/G = 1.75$ at 93.60 GPa

for $P3m1$-BC_7. The v of $P3m1$-BC_7 and $Pmm2$-BC_7 as a function of pressure are also depicted in Fig. 4a with v increases observed with increasing pressure, $B/G = 1.75$ at 93.60 GPa and v =0.26 at 93.73 GPa for $P3m1$-BC_7. $P3m1$-BC_7 is found to turn brittle to ductile in this pressure range, while $Pmm2$-BC_7 remains brittle.

Anisotropy of elasticity exerts significant implications in engineering science and crystal physics, thus anisotropy of $P3m1$-BC_7 and $Pmm2$-BC_7 is investigated. Shear anisotropic factors measure a degree of anisotropy in the bonding between atoms in different planes. The shear anisotropic factor for {100} shear planes between ⟨011⟩ and ⟨010⟩ directions is [32, 33]:

$$A_1 = \frac{4C_{44}}{C_{11} + C_{33} - 2C_{13}}, \tag{11}$$

for the {010} shear planes between ⟨101⟩ and ⟨001⟩ directions [32, 33];

$$A_2 = \frac{4C_{55}}{C_{22} + C_{33} - 2C_{23}}, \tag{12}$$

for the {001} shear planes between ⟨110⟩ and ⟨010⟩ directions [32, 33];

$$A_3 = \frac{4C_{66}}{C_{11} + C_{22} - 2C_{12}}. \tag{13}$$

The factors A_1, A_2, and A_3 must be one for isotropic crystal, while any value smaller or greater than one is a measure of the elastic anisotropy possessed by the crystal. The anisotropy factors of $P3m1$-BC_7 and $Pmm2$-BC_7 as a function of pressure are displayed in Fig. 4b. A_1 of $P3m1$-BC_7 obviously decreases as C_{44} decreases 24.84% from 0 GPa to 10 GPa and A_1 of $P3m1$-BC_7 decreases at $P = 10$ GPa while A_3 of $P3m1$-BC_7 remains nearly constant. Elastic anisotropic of $Pmm2$-BC_7 is greater than $P3m1$-BC_7 (Fig. 4b). Generally, the universal elastic anisotropy index (A^U) is derived from the B and G of the Voigt and Reuss bounds as the formula $A^U = 5(G_V/G_R) + (B_V/B_R) - 6$. The A^U of $P3m1$-BC_7 and $Pmm2$-BC_7 were calculated as a function with pressure. $A^U(P3m1) = 0.269$, $A^U(Pmm2) = 0.300$ at 0 GPa, and $A^U(P3m1) = 0.554$, $A^U(Pmm2) = 0.678$ at 100 GPa, respectively. Moderate deviations of the index from standard value ($A^U = 0$) imply considerable elastic anisotropy of $P3m1$-BC_7 and $Pmm2$-BC_7 while elastic properties comparisons indicate that $Pmm2$-BC_7 exhibits slightly higher values in A^U.

Utilizing ELAM [34], the calculated Poisson ratio, shear modulus, and the Young modulus along different directions, including projections in different planes, may be obtained in Fig. 5 and Fig. 6. Figure 5a–c displays the 2D representation of the Poisson ratio in the xy, xz, and yz planes for $P3m1$-BC_7 and $Pmm2$-BC_7, respectively. Relatively large anisotropy in the Poisson ratio is found as indicated in the figures. Shear modulus for all directions of shear strain were also calculated to quantify the anisotropy. 2D representation of shear modulus in the xy, xz, and yz planes for $P3m1$-BC_7 and $Pmm2$-BC_7 are displayed in Fig. 5d–f, respectively. The calculated maximum result of shear modulus for $P3m1$-

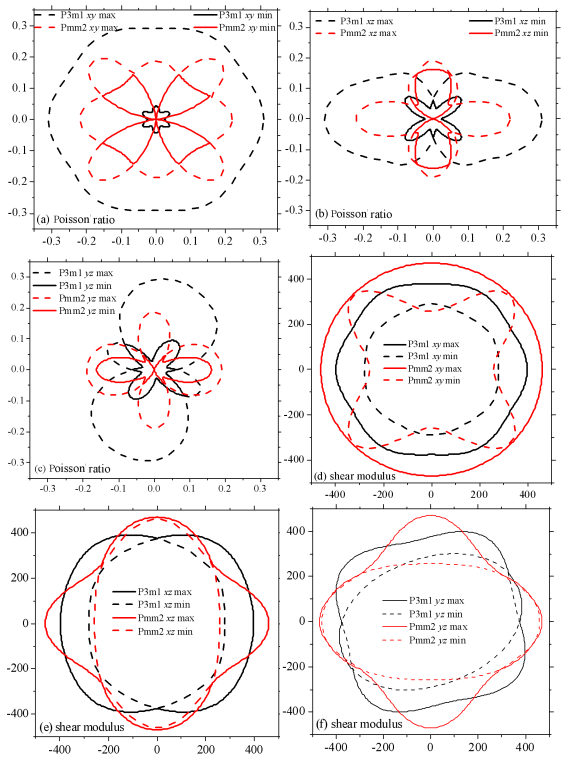

Fig. 5. 2D representation of the Poisson ratio and shear modulus in the xy plane (a,d), xz plane (b,e) and yz plane (c,f) for $P3m1$-BC_7 and $Pmm2$-BC_7, respectively.

BC_7 and $Pmm2$-BC_7 are 440 GPa and 470 GPa, respectively, while the calculated minimal result of shear modulus for $P3m1$-BC_7 and $Pmm2$-BC_7 is 279 GPa and 257 GPa, respectively. Ratios $G_{\max}/G_{\min}(P3m1) = 1.58$ and $G_{\max}/G_{\min}(Pmm2) = 1.83$ also indicate $Pmm2$-BC_7 exhibits a large elastic anisotropy. The directional dependence of the Young modulus for $P3m1$-BC_7 and $Pmm2$-BC_7 are presented in Fig. 6a and c, respectively. Figure 6b and d demonstrates 2D representation of shear modulus in the xy, xz, and yz planes for $P3m1$-BC_7 and $Pmm2$-BC_7. The 704 GPa $< E_{P3m1} <$ 1093 GPa, 648 GPa $< E_{Pmm2} <$ 989 GPa, and the average value of all directions is 876 GPa and 847 GPa for $P3m1$-BC_7 and $Pmm2$- BC_7, respectively. The Young modulus 3D figure for the $P3m1$-BC_7 exhibits more anisotropic characteristics along the z-axis than that along the x-axis.

3.3. Hardness

The formula for the Knoop hardness [35] (in GPa) was utilized to calculate hardness H_v:

$$H_v = \frac{423.8}{V} n \sqrt[n]{\prod_{k=1}^{n} N_k X_k \, \mathrm{e}^{-2.7 f_k}} - 3.4, \tag{14}$$

where V is the volume of the unit cell and N_k is the number of bonds of the type k in the unit cell. X_k and f_k represent electron-holding energy of the bond k and the iconicity indicator, defined as in the original work of Li et al. [36]:

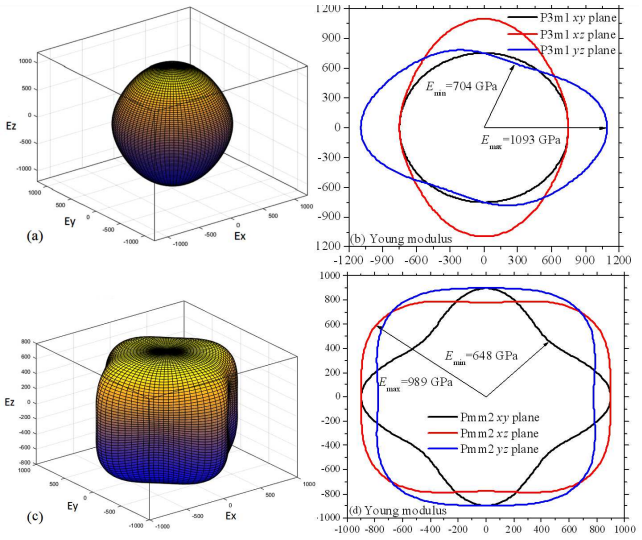

Fig. 6. The directional dependence of the Young modulus for $P3m1$-BC_7 (a) and $Pmm2$-BC_7 (c), 2D representation of the Young modulus for $P3m1$-BC_7 (b) and $Pmm2$-BC_7 (d).

$$X_k = \sqrt{\frac{\chi_i^k \chi_j^k}{CN_i^k CN_j^k}}, \tag{15}$$

$$f_k = \frac{\left|\chi_i^k - \chi_j^k\right|}{4\sqrt{\chi_i^k \chi_j^k}}, \tag{16}$$

χ_i^k, χ_j^k denote the electronegativity of atoms i, j in bonds. CN_i^k, CN_j^k are the coordination numbers of atoms i and j. Bond valence (s) is computed utilizing the classical Brown bond valence model [37]:

$$s_i^k = \frac{v_i \exp(-\Delta_k/0.37)}{\sum_{k'} \exp(-\Delta_{k'}/0.37)}. \tag{17}$$

Denoted by n are the number of different bond types in the unit cell, as labeled with the index $k = [1 \div n]$. The model [36] computes the electronegativity of each i-th atom as $\chi = 0.481 n_i/R_i$ where n_i and R_i represent the number of valence electrons and univalent covalent radius of the atom, respectively. The sum applies to all bonds k' where atom i participates, and Δ represents deviation from reference covalent bond length. The definition satisfies the sum rule exactly:

$$\sum_{k'} s_i^{k'} = v_i. \tag{18}$$

Use of the multicolor graph theory is the most defining feature of the Lyakhov–Oganov approach, i.e. bond topology is utilized, in addition to bond strengths, for computing hardness. The weak bonds for molecular, chain and layered structures, defining crystal hardness, also maintain three dimensionality.

The output file contains the following information: length symbolizes bond modulus, Delta (Δ) is a deviation from bond length defined by the reference univalent covalent radius, N^k is number of type k bonds in the unit cell, and s_i and s_j represent bond valence.

TABLE III

Calculated hardness of BC_7 and diamond.

	bond	length	Δ_k	N_k	s_i	s_j	$X_k\, e_k^{-2.7f}$	Hv
P3m1	B-C	1.607	0.007	4	0.750	0.970	1.571	
	C-C	1.473	-0.047	1	1.167	1.098	0.739	
	C-C	1.543	0.023	11	1.005	0.982	6.809	51.4
Pmm2	B-C	1.611	0.011	4	0.750	0.996	1.589	
	C-C	1.538	0.018	12	1.001	1.000	7.508	59.8
P-4m2	B-C	1.648	0.048	4	0.956	0.750	1.524	
	C-C	1.546	0.026	12	1.010	1.005	7.518	56.8
P-43m	B-C	1.601	0.001	4	1.072	0.750	1.658	
	C-C	1.556	0.036	12	0.996	0.980	7.329	58.9
diamond	C-C	1.544	0.024	16	1.000	1.000	9.966	89.7,91.2[a], 90[b]

[a] Ref [35], [b] Exp., Ref [38]

Calculated hardness of $P3m1$-BC_7, $Pmm2$-BC_7, P-4$m2$-BC_7, P-43m-BC_7 and diamond via the approach is listed in Table III. The calculated hardness of diamond is 89.7 GPa, in alignment with the reported experimental result (90 GPa [38]). $Pmm2$-BC_7 retains superior hardness over other BC_7 in the BC_7 system with order of hardness (for the considered BC_7 compounds) as $Pmm2 > P$-43$m > P$-4$m2 > P3m1$.

3.4. Thermodynamic properties

Thermodynamic properties of solids at high pressure and at high temperature are noteworthy, within condensed matter physics. Thermodynamics calculations are necessary to acquire the corresponding properties as functions of temperature and pressure in terms of the quasi-harmonic Debye model [39–43], as applied to estimate thermodynamic properties of various materials [29, 43]. The coefficient of thermal expansion α demonstrates the relationship between object size and temperature change. The coefficients of thermal expansion for $P3m1$-BC_7 and $Pmm2$-BC_7 are plotted as a function of pressure and temperature (Fig. 7a and b) and are found to increase with increase of temperature and decrease of pressure. Additionally, the coefficient of thermal expansion versus pressure exhibits a near linear relation at a given lower temperature ($T < 500$ K). Two-dimensional contour plots of the Grüneisen parameter γ, versus pressure and temperature for $P3m1$-BC_7 and $Pmm2$-BC_7 are displayed in both Fig. 7c and d. The Grüneisen parameter γ describes the effect on vibrational properties of changing the crystal lattice volume and, as a consequence, the effect of changing temperature on the size or dynamics of the lattice. Effect of the temperature T on the coefficient of thermal expansion is more significant than pressure P (Fig. 7), and in contrast with the Grüneisen parameter effect, pressure P is greater.

Two-dimensional contour plots illustrating dependence of the Debye temperature on pressure and temperature for $P3m1$-BC_7 and $Pmm2$-BC_7 are displayed in Fig. 8. The Deybe temperature is affected by both pressure and temperature and the effect of increase of temperature on $P3m1$-BC_7 and $Pmm2$-BC_7 is the same as decrease of pressure. The Debye temperature decreases quickly at a given temperature with increase of pressure and typically,

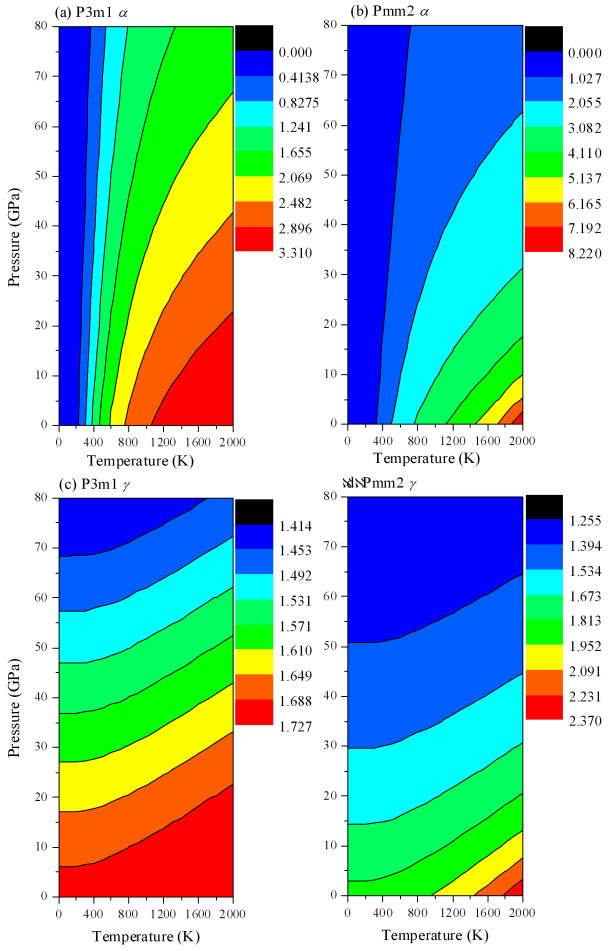

Fig. 7. Two-dimensional contour plots of coefficient of thermal expansion and Grüneisen parameter versus pressure and temperature for $P3m1$-BC_7 (a, c) and $Pmm2$-BC_7 (b, d).

the higher Debye temperature, the greater material microhardness. The resulting Debye temperature is 1797 K and 1878 K for $P3m1$-BC_7 and $Pmm2$-BC_7, which aligns with the previous description.

Heat capacity, or thermal capacity, is a measurable physical quantity equal to the ratio of heat added to (or subtracted from) an object to the resulting temperature change. The two-dimensional contour plots indicating dependence of heat capacity on pressure and temperature for $P3m1$-BC_7 and $Pmm2$-BC_7 are displayed in Fig. 9, with heat capacity as a function of temperature at various pressures. Heat capacity at constant pressure (C_P) and at constant volume (C_V) follows the law of T^3 as expected in the range from 0 K to 800 K, considered as low temperatures with respect to the large Debye temperature of $P3m1$-BC_7 and $Pmm2$-BC_7. C_V and C_P then expand with increase of temperature at a given pressure and decrease with increase of pressure at a given temperature. The C_V of $P3m1$-BC_7 and $Pmm2$-BC_7 increases slowly at high temperature up to 1600 K, due to the high Debye temperature, they tend to achieve limitations in accordance with the Dulong–Petit law.

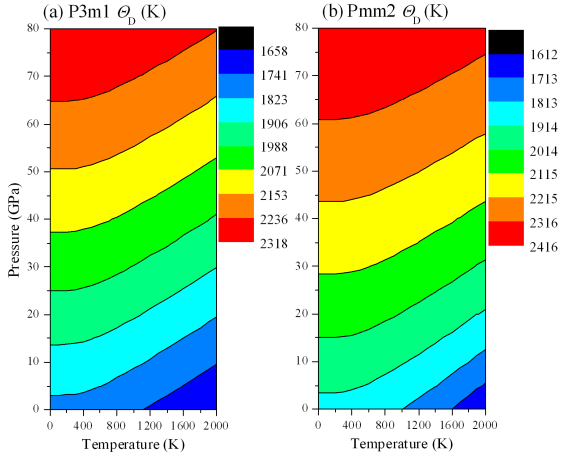

Fig. 8. Two-dimensional contour plots of the Debye temperature versus pressure and temperature for $P3m1$-BC_7 (a) and $Pmm2$-BC_7 (b).

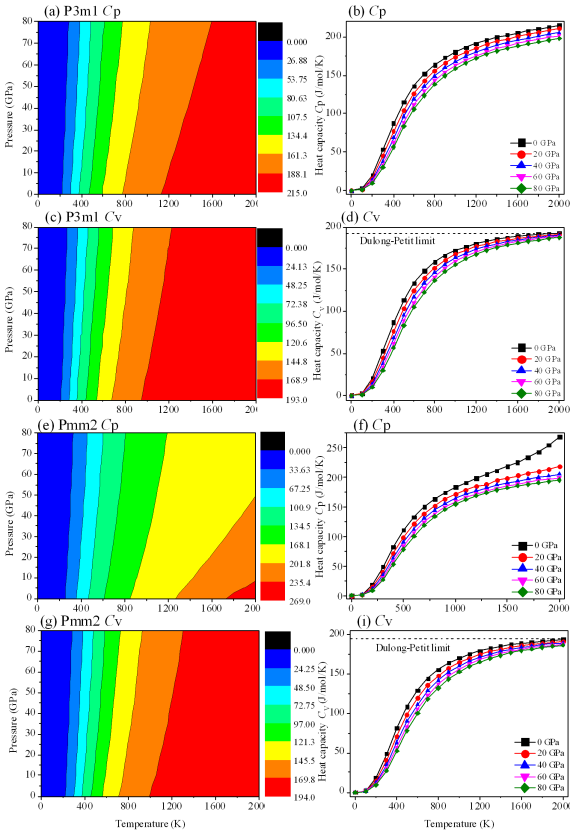

Fig. 9. Calculated specific volume C_V and pressure heat capacity C_P as a function of pressure for $P3m1$-BC_7 and $Pmm2$-BC_7 at different temperature: C_P contours (a, e), C_P–T (b, f), C_V contours (c, g), and C_V–T (d, i), respectively.

4. Conclusions

A detailed investigation of the structural, elastic, and anisotropic properties of $P3m1$-BC_7 and $Pmm2$-BC_7 utilizing the DFT within the ultrasoft pseudopotential scheme in the frame of GGA and LDA was conducted in this study. The elastic anisotropy of $P3m1$-BC_7 and

$Pmm2$-BC_7 are discussed in detail under pressure from 0 GPa to 100 GPa. The calculated Pugh modulus ratio (B/G) and the Poisson ratio indicate transition of $P3m1$-BC_7 from brittle to ductile at approximately 93.68 GPa. The A_1, A_2, A_3, A^U, the shear modulus, the Young modulus, and the Poisson ratio for $P3m1$-BC_7 and $Pmm2$-BC_7 reveal that $Pmm2$-BC_7 exhibits a larger elastic anisotropy than $P3m1$-BC_7. Thermodynamic properties of $P3m1$-BC_7 and $Pmm2$-BC_7, including the Debye temperature, heat capacity, and thermal expansion and the Grüneisen parameters are researched through application of the quasi-harmonic Debye model.

Acknowledgments

This work was supported by the Fund for Talents of Yunnan Province, China (Grant No. KKSY201403006) and the National Natural Science Foundation of China (No. 61564005).

References

[1] R.B. Kaner, J.J. Gilman, S.H. Tolbert, *Science* **308**, 1268 (2005).

[2] V.L. Solozhenko, O.O. Kurakevych, D. Andrault, Y. Le Godec, M. Mezouar, *Phys. Rev. Lett.* **102**, 015506 (2009).

[3] M. Calandra, F. Mauri, *Phys. Rev. Lett.* **101**, 016401 (2008).

[4] C. Jiang, Z.J. Lin, Y.S. Zhao, *Phys. Rev. B* **80**, 184101 (2009).

[5] Y.C. Liang, W.Q. Zhang, J.Z. Zhao, L.F. Chen, *Phys. Rev. B* **80**, 113401 (2009).

[6] Y.S. Yao, J.S. Tse, D.D. Klug, *Phys. Rev. B* **80**, 094106 (2009).

[7] J.E. Lowther, 17, 3221 *J. Phys. Condens. Matter* , (2005).

[8] Q.A. Li, H. Wang, Y.J. Tian, Y. Xia, T.A. Cui, J.L. He, Y.M. Ma, G.T. Zou, *J. Appl. Phys.* **108**, 5 (2010).

[9] P.V. Zinin, L.C. Ming, I. Kudryashov, N. Konishi, S.K. Sharma, *J. Raman Spectrosc.* **38**, 1362 (2007).

[10] P.V. Zinin, L.C. Ming, I. Kudryashov, N. Konishi, M.H. Manghnani, S.K. Sharma, *J. Appl. Phys.* **100**, 013516 (2006).

[11] E.A. Ekimov, V.A. Sidorov, E.D. Bauer, N.N. Mel'nik, N.J. Curro, J.D. Thompson, S.M. Stishov, *Nature* **428**, 542 (2004).

[12] J.E. Moussa, M.L. Cohen, *Phys. Rev. B* **77**, 064518 (2008).

[13] V.L. Solozhenko, O.O. Kurakevych, D. Andrault, Y. Le Godec, M. Mezouar, *Phys. Rev. Lett.* **102**, 015506 (2009).

[14] L.F. Xu, Z.S. Zhao, Q.Q. Wang, L.M Wang, B. Xu, J.L. He, Y.J. Tian, *J. Appl. Phys.* **110**, 013501 (2011).

[15] M. Zhang, H.Y. Liu, Q. Li, B. Gao, Y.C. Wang, H.D. Li, C.F. Chen, Y.M. Ma, *Phys. Rev. Lett.* **114**, 015502 (2015).

[16] W.J. Zhao, Y.X. Wang, *Solid State Commun.* **151**, 478 (2011).

[17] H.Y. Liu, Q. Li, L. Zhu, Y.M. Ma, *Phys. Lett. A* **375**, 771 (2011).

[18] H.Y. Liu, Q. Li, L. Zhu, Y.M. Ma, *Solid State Commun.* **151**, 716 (2011).

[19] P. Hohenberg, W. Kohn, *Phys. Rev.* **136**, B864 (1964).

[20] W. Kohn, L.J. Sham, *Phys. Rev.* **140**, A1133 (1965).

[21] J.P. Perdew, K. Burke, M. Ernzerhof, *Phys. Rev. Lett.* **77**, 3865 (1996).

[22] D.M. Ceperley, B.J. Alder, *Phys. Rev. Lett.* **45**, 566 (1980).

[23] J.P. Perdew, A. Zunger, *Phys. Rev. B* **23**, 5048 (1981).

[24] S.J. Clark, M.D. Segall, C.J. Pickard, P.J. Hasnip, M.I.J. Probert, K. Refson, M.C. Payne, *Z. Kristallogr.* **220**, 567 (2005).

[25] H.J. Monkhorst, J.D. Pack, *Phys. Rev. B* **13**, 5188 (1976).

[26] F. Birch, *J. Geophys. Res. Solid Earth* **83**, 1257 (1978).

[27] Q.Y. Fan, Q. Wei, C.C. Chai, H.Y. Yan, M.G. Zhang, Z.Z. Lin, Z.X. Zhang, J.Q. Zhang, D.Y. Zhang, *J. Phys. Chem. Solids* **79**, 89 (2015).

[28] J.F. Nye, *Physical Properties of Crystals*, Oxford University Press, Oxford 1985.

[29] Q.Y. Fan, Q. Wei, H.Y. Yan, M.G. Zhang, D.Y. Zhang, J.Q. Zhang, *Acta Phys. Pol. A* **126**, 740 (2014).

[30] J.J. Lewandowski, W.H. Wang, A.L. Greer, *Philos. Mag. Lett.* **85**, 77 (2005).

[31] S.F. Pugh, *Philos. Mag.* **45**, 823 (1954).

[32] D. Connétable, O. Thomas, *Phys. Rev. B* **79**, 094101 (2009).

[33] Q.Y. Fan, Q. Wei, H.Y. Yan, M.G. Zhang, Z.X. Zhang, J.Q. Zhang, D.Y. Zhang, *Comput. Mater. Sci.* **85**, 80 (2014).

[34] A. Marmier, Z.A.D. Lethbridge, R.I. Walton, C.W. Smith, S.C. Parker, K.E. Evans, *Comput. Phys. Commun.* **181**, 2102 (2010).

[35] A.O. Lyakhov, A.R. Oganov, *Phys. Rev. B* **84**, 092103 (2011).

[36] K. Li, X. Wang, F. Zhang, D. Xue, *Phys. Rev. Lett.* **100**, 235504 (2008).

[37] I.D. Brown, *Acta Crystallogr. B* **48**, 553 (1992).

[38] C.A. Brookes, E.J. Brookes, *Diamond Relat. Mater.* **1**, 13 (1991).

[39] M.A. Blanco, E. Francisco, V. Luaña, *Comput. Phys. Commun.* **158**, 57 (2004).

[40] Q.Y. Fan, C.C. Chai, Q. Wei, Y.T. Yang, Q. Yang, P.Y. Chen, M.J. Xing, J.Q. Zhang, R.H. Yao, *J. Solid State Chem.* **233**, 471 (2016).

[41] F. Peng, H.Z. Fu, X.L. Cheng, *Physica B* **400**, 83 (2007).

[42] Q.Y. Fan, Q. Wei, C.C. Chai, H.Y. Yan, M.G. Zhang, Z.X. Zhang, J.Q. Zhang, D.Y. Zhang, *Ind. J. Pure Appl. Phys.* **54**, 227 (2016).

[43] M.J. Xing, B.H. Li, *Chin. J. Phys.* **52**, 1812 (2014).